IOPscience iopscience.iop.org

Home Search Collections Journals About Contact us My IOPscience

Significantly reduced thermal diffusivity of free-standing two-layer graphene in graphene foam

This content has been downloaded from IOPscience. Please scroll down to see the full text.

2013 Nanotechnology 24 415706

(http://iopscience.iop.org/0957-4484/24/41/415706)

View the table of contents for this issue, or go to the journal homepage for more

Download details:

IP Address: 75.167.93.18
This content was downloaded on 25/09/2013 at 03:09

Please note that terms and conditions apply.

Nanotechnology **24** (2013) 415706 (10pp) doi:10.1088/0957-4484/24/41/415706

Significantly reduced thermal diffusivity of free-standing two-layer graphene in graphene foam

Huan Lin[1,2,3], **Shen Xu**[1,3], **Xinwei Wang**[1] **and Ning Mei**[2]

[1] Department of Mechanical Engineering, Iowa State University, 2010 Black Engineering Building, Ames, IA 50011, USA
[2] College of Engineering, Ocean University of China, Qingdao, Shandong 266100, People's Republic of China

E-mail: xwang3@iastate.edu

Received 17 July 2013, in final form 29 August 2013
Published 23 September 2013
Online at stacks.iop.org/Nano/24/415706

Abstract
We report on a thermal diffusivity study of suspended graphene foam (GF) using the transient electro-thermal technique. Our Raman study confirms the GF is composed of two-layer graphene. By measuring GF of different lengths, we are able to exclude the radiation effect. Using Schuetz's model, the intrinsic thermal diffusivity of the free-standing two-layer graphene is determined with a high accuracy without using knowledge of the porosity of the GF. The intrinsic thermal diffusivity of the two-layer graphene is determined at 1.16–2.22 $\times 10^{-4}$ m^2 s^{-1}. The corresponding intrinsic thermal conductivity is 182–349 W m^{-1} K^{-1}, about one order of magnitude lower than those reported for single-layer graphene. Extensive surface impurity defects, wrinkles and rough edges are observed under a scanning electron microscope for the studied GF. These structural defects induce substantial phonon scattering and explain the observed significant thermal conductivity reduction. Our thermal diffusivity characterization of GF provides an advanced way to look into the thermal transport capacity of free-standing graphene with high accuracy and ease of experimental implementation.

(Some figures may appear in colour only in the online journal)

1. Introduction

Graphene is a two-dimensional monolayer of carbon atoms packed into a honeycomb lattice that possesses much new physics [1, 2] and many unique properties, such as extraordinarily high electron mobility [3], extremely high thermal conductivity [4], ultra-large specific surface area [5] and extraordinary elasticity and stiffness [6]. Owing to these fascinating properties, in the past few years since its discovery, graphene has been widely applied in microelectronic devices [7], transparent conductors [8], biological/chemical sensors [9], electrodes for energy storage [10] and conversion [11] devices, and fillers in conductive polymeric composites [12], etc. We point out that there are many references about graphene, some of which we cite in this work.

As a promising candidate for nanoelectronics devices, graphene has attracted much attention in research in recent years. It demonstrates not only specific electronic properties [13], but also very high thermal conductivity. In 2008, it was discovered that graphene has an extremely high intrinsic thermal conductivity, exceeding that of CNTs [4, 14–16]. The excellent heat-conduction property of graphene is beneficial for many potential applications. For example, graphene lying on solid substrates can be patterned and interconnected for field-effect transistor applications [17]. Few-layer graphene (FLG) heat spreaders are shown to substantially reduce the temperature rise in high-power

[3] Authors contributed equally.

 © 2013 IOP Publishing Ltd Printed in the UK & the USA

GaN field-effect transistors [18]. The potential use of graphene in polymer composites for thermal management and thermal conductivity enhancement has been explored [19, 20]. The demonstrated thermal conductivity enhancement of composites by the addition of small volume fractions of liquid-phase exfoliated graphene is promising for thermal interface materials (TIM) applications [14, 20]. Shahil *et al* [20] found that the optimized mixture of graphene and multilayer graphene, produced by the high-yield inexpensive liquid-phase-exfoliation technique, can lead to an extremely strong enhancement of the cross-plane thermal conductivity of the composite. Yu *et al* [21] found that nanofluids containing graphene oxide nanosheets (GONs) have higher thermal conductivities than the base fluids. Soujit *et al* [22] measured the thermal conductivity of nanofluids containing graphene nanosheets (GnS) by using the transient hot wire method. It was found that the thermal conductivity is substantially enhanced even at lower concentrations and the enhancement improves with increasing concentration.

The first experimental studies of the thermal conductivity (k) of graphene were carried out at University of California Riverside [4, 14–16, 23] using an original non-contact Raman optothermal technique. It was found that graphene has an extremely high intrinsic k, exceeding that of CNTs. Recently, micro-Raman spectroscopy-based techniques [24] and micro-resistance thermometry [25] have been employed to measure k of graphene, in the range 1500–5800 W m^{-1} K^{-1} for suspended single-layer graphene (SLG) [26], and 600 W m^{-1} K^{-1} for supported SLG at near room temperature (RT) due to flexural phonon coupling with the SiO_2 substrate [27]. Meanwhile, theoretical studies on thermal transport in graphene have focused on solutions of the linearized Boltzmann transport equation (BTE) [28] and molecular dynamics (MD) simulations [29]. Nika *et al* [16] performed a detailed numerical study of the lattice thermal conductivity of graphene using the phonon dispersion obtained by the valence-force field (VFF) method. It was found that the near room temperature thermal conductivity of SLG is in the range 2000–5000 W m^{-1} K^{-1}, depending on the flake width, defect concentration and roughness of the edges. Owing to the long phonon mean free path, graphene edges have a strong effect on thermal conductivity even at RT [16]. Lan *et al* [30] determined the thermal conductivity of graphene nanoribbons by combining the tight-binding approach and the phonon nonequilibrium Green's function method. They found that at RT the thermal conductivity is 3410 W m^{-1} K^{-1}.

Three-dimensional (3D) macroporous graphene nanostructures can be constructed by graphene nanosheets through template-directed CVD [31] or templated assembly [32] methods. 3D graphene possesses fascinating properties, such as a large surface area, high conductivity of the graphene matrix, low mass transport resistance, high specific capacity and good cycle stability at high current densities. 3D graphene foams (GF) are seamlessly continuous and free of defects and inter-sheet junctions. Their unique morphology and porous structure make them good candidates as the scaffold for the fabrication of monolithic composite electrodes [33]. GF structures are highly sensitive to the chemical environment and offer ultra-high sensitivity for chemicals [34]. The GF with a certain degree of mechanical strength could be self-supported. Though the graphene framework is very thin, and is translucent under electron beams, the ultra-high mechanical strength of graphene sheets gives rise to the macroscopic elasticity of the foam-like structure [35]. Very recently, Pettes *et al* [36] measured the temperature-dependent electron and phonon transport of 3D GF structures consisting of FLG and ultrathin graphite (UG) synthesized through the use of methane chemical vapor deposition (CVD) on open-celled reticulated nickel foam. A steady-state method is used to measure the thermal conductivity of GF. Then, based on a theoretical model and the density of the foam, the solid thermal conductivity of the FLG and UG constituents was evaluated. They established the relationship between the processing conditions and the transport properties of free-standing GF structures. Their measurement results showed that the structure quality and transport properties of the free-standing GF depend much more sensitively on the etching process of the sacrificial Ni foam than on the grain size of the Ni foam. They found the effective thermal conductivity of GF is limited by the very low GF volume fraction instead of the internal contact thermal resistance. The solid thermal conductivity of the FLG and UG constituents reached about 1600 W m^{-1} K^{-1} at 150 K.

In this work, we use the transient electro-thermal (TET) technique developed in our laboratory to characterize the thermal diffusivity of 3D GF composed of two-layer graphene. Our unique thermal diffusivity characterization makes it possible to directly evaluate the thermal conductivity of the free-standing graphene without requiring knowledge of the porosity (density) of the GF. The three-dimensional, porous and cross-linked network structure and honeycomb-like surface of GF are clearly observed in our samples, and will be discussed later. Such a continuous network mainly consists of free-standing graphene and gives a great platform to study the physical properties of graphene. Section 2 details the GF material and its structure. Section 3 describes the method developed for measuring the thermal conductivity of the suspended graphene foam. In section 4, we provide details of the measurements, our results, and a discussion.

2. Materials and structure

The three-dimensional free-standing GF sample used in the thermal measurement was obtained from Advanced Chemicals Supplier (ACS) Material Company. They use a scaffold of porous nickel foam as a template for the deposition of graphene to fabricate the GF. Chemical vapor deposition (CVD) is used to deposit carbon atoms on the nickel foam using CH_4 decomposition at ∼1000 °C under ambient pressure. The nickel scaffold is then removed by chemical etching using a hot HCl (or $FeCl_3$) solution. A thin layer of poly (methyl methacrylate) (PMMA) is also deposited on the surface of the graphene formed on the nickel foam to maintain the integrity of the foam during the etching of Ni and prevent it from collapsing. In the final step

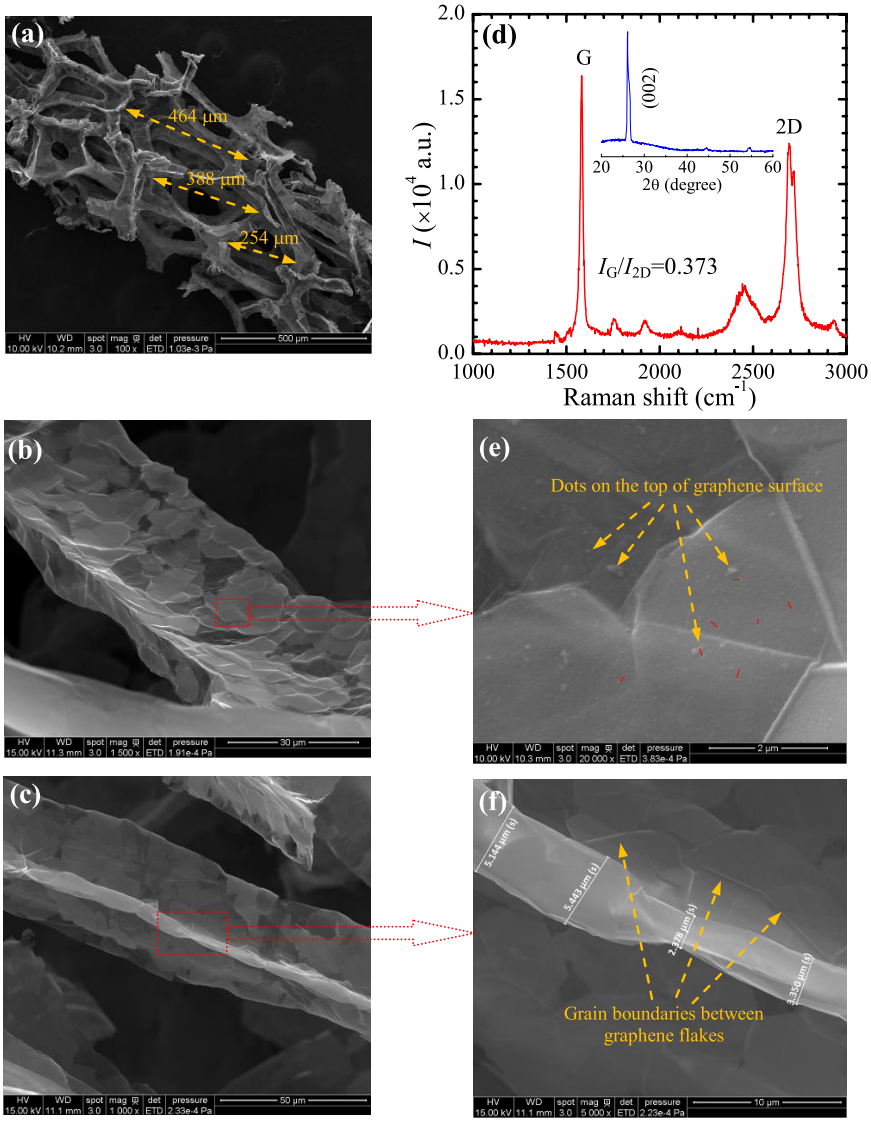

Figure 1. SEM and Raman spectra images of GF studied in this work. (a)–(c), (e) and (f) SEM images of GF from low to high resolutions. (d) Raman spectrum of the GF sample. I_G/I_{2D} is the ratio of the integrated intensity of the G band to that of the 2D band. The inset in (d) is the x-ray diffraction spectrum of GF. The red lines in (e) indicate the distance between dots on the graphene surface.

the PMMA layer is dissolved by hot acetone, resulting in a free-standing three-dimensional graphene network structure. More details regarding the process are provided in [31]. Figure 1 shows scanning electron microscopy (SEM) images and the Raman spectrum of GF studied in our work. Three-dimensional, porous and cross-linked network structure and honeycomb-like surface of GF can be clearly observed in figure 1(a). From this figure we can also see that inside the foam there are many spherical pores with small openings (their size around 200–500 μm). These pores are three-dimensionally interconnected by graphene flakes. Such a network structure can also be clearly observed under an optical microscope, as shown in figure 2(b). We use energy dispersive spectroscopy (EDS) to identify the element composition of the GF sample. The result shows that our GF sample is very pure and the primary composition is carbon (96.72 wt%), oxygen (1.28 wt%) and phosphorus (0.34 wt%).

The 3D GF is also characterized using Raman spectroscopy. A confocal Raman spectrometer (Voyage, B&W Tek, Inc.) installed with a 532 nm excitation laser and a microscope (Olymoys BX51) is employed to focus the laser. The spectral resolution is 1–2 cm^{-1}. The graphene sample, which is the same one as used in the SEM images, is mounted on a three-dimensional nanostage (Max 311D). During the measurement, a 100× microscope objective is used to focus the laser beam to a spot of about 0.5 μm in diameter. Since the foam structure has many layers, we just focus on its top surface to get the Raman spectrum—the result is shown in figure 1(d). To ensure a sound spectrum, the integration time is set to 60 s with five repeated scans. The laser energy is 8.6×10^8 W m^{-2} in this measurement.

In figure 1(d), this GF clearly shows two major peaks, 1581 cm^{-1} (G band) and 2694 cm^{-1} (2D band). The G band (around 1580 cm^{-1}) is the primary peak in graphite materials, including graphene and other carbon nanomaterials,

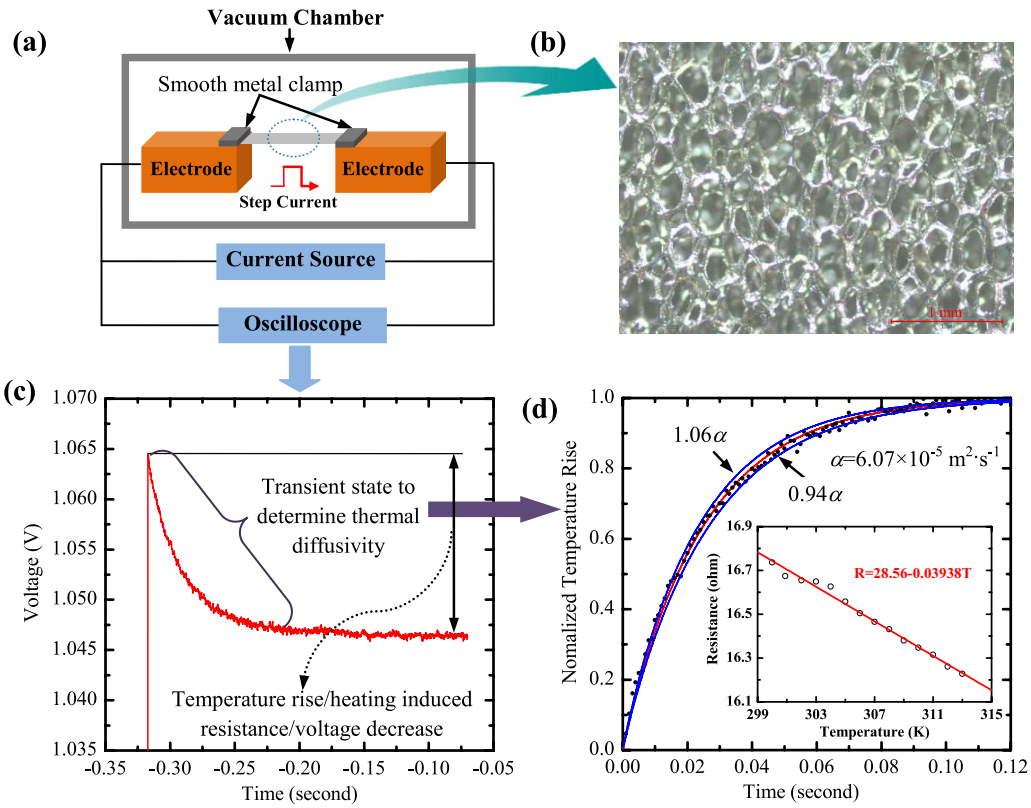

Figure 2. (a) Schematic of the experimental principle and the step current provided for the TET technique. (b) Optical microscopy image of a GF sample connected between two electrodes. (c) Experimental data (voltage variation against time) for one GF (sample 1). When the temperature increases the resistance decreases for the GF sample. Therefore, the temperature rise reflected by a resistance/voltage decrease can be used to determine the thermal diffusivity. (d) Comparison between theoretical fitting and experimental data for the normalized temperature rise versus time (sample 1). The inset shows the linear fitting of the resistance change against temperature for one general GF sample (1.1 mm wide, 4.17 mm long and 0.87 mm thick).

and represents the sp^2 planar carbon configuration. The 2D band (around 2700 cm^{-1}) is the feature peak of few-layer graphene and is a result of a two-phonon lattice vibration mode [37]. The ratio of the integrated intensities of the G band to that of the 2D band is calculated through fitting these two peaks, which can be used to determine the approximate number of layers of graphene. The ratio is 0.373 for our sample. According to previous work [38], there should be two-layer graphene in our GF. X-ray diffraction (XRD) analysis of the GF is conducted to study its structure—the result is shown in the inset of figure 1(d). The interlayer spacing revealed by peak (002) is 3.3940 Å, very close to 3.3553 Å reported for highly oriented pyrolytic graphite [39]. The asymmetric shape of the (002) peak in the XRD spectrum is caused by the 3D structure of the graphene foam. When the x-rays irradiating the (002) face are not parallel to the sample surface, some Bragg diffraction will scatter in directions other than to the detector. As a result the (002) peak in the XRD spectrum cannot be fitted with an accurate full-width at half-maximum [40].

3. Methods for thermal characterization

The transient electro-thermal (TET) technique is an effective, accurate, and fast approach developed in our lab to measuring the thermal diffusivity of solid materials, including conductive, semi-conductive or non-conductive one-dimensional structures. The measurement accuracy of this technique has been fully examined by characterizing known materials, both metallic and dielectric. The TET measurement results agree with reference values with less than 5% difference. Guo *et al* have used this technique to measure the thermal diffusivity of micro-scale polyester fibers [41] and micro/nanoscale polyacrylonitrile fibers [42]. Furthermore, Feng *et al* have employed the TET technique to measure the thermal diffusivity of thin films composed of anatase TiO_2 nanofibers [43], single anataseTiO_2 nanowires [44] and free-standing micrometer-thick Poly (3-hexylthiophene) films [45]. Sound agreement has been obtained between these measured thermal diffusivities and the reference values. Huang *et al* [46] have extended the TET technique and measured the thermophysical properties of multi-wall carbon nanotube bundles at elevated temperatures up to 830 K.

The TET technique is used in this work for thermal characterization of GF. A schematic of the TET experiment setup is shown in figure 2(a). In the experiment, the sample is suspended between two copper electrodes. Small silicon pieces or smooth metal pieces are clamped at the sample-electrode contact to reduce the thermal and electrical

contact resistances to a negligible level. The whole sample is placed in a vacuum chamber to reduce heat transfer to the air. During measurement, a step current is fed through the sample to induce Joule heating. Upon this step current Joule heating, the sample will experience a quick temperature increase. The temperature change of the wire will induce an electrical resistance change, which leads to an overall voltage change of the wire. How fast/slow the temperature increases is determined by two competing processes: one is the Joule heating, and the other one is the heat conduction from the sample to the electrodes. A higher thermal diffusivity of the sample will lead to a faster temperature evolution, meaning a shorter time to reach the steady state. Therefore, the transient voltage/temperature change can be used to determine the thermal diffusivity. When determining the thermal diffusivity of the sample, no real temperature rise is needed. In fact, only the normalized temperature rise based on the voltage decrease is needed. The induced voltage–time (V–t) profile recorded by the oscilloscope is presented in figure 2(c). Processes for determining the thermal diffusivity and thermal conductivity are outlined below.

For the GF samples in this work, as their dimensions are much larger than the pore size within the foam (200–500 μm), we can assume that the volumetric heat generation due to Joule heating is uniform in space. So the heat conduction can be taken as one-dimensional in the GF sample length direction. During TET thermal characterization, the surface radiation effect could be significant if the sample has a very large aspect ratio (L/D, D: thickness of sample). The heat transfer rate of radiation from the sample surface can be expressed as:

$$\begin{aligned} Q_{\mathrm{rad}} &= \varepsilon_{\mathrm{r}}\sigma A_{\mathrm{s}}(T^4 - T_0^4) \\ &= 2\varepsilon_{\mathrm{r}}\sigma WL(4T_0^3\theta + 6T_0^2\theta^2 + 4T_0\theta^3 + \theta^4), \end{aligned} \quad (1)$$

where ε_{r} is the effective emissivity of the sample, $\sigma = 5.67 \times 10^{-8}$ W m^{-2} K^{-4} is the Stefan–Boltzmann constant, A_{s} the surface area, T the surface temperature, L the length, T_0 the temperature of the environment (vacuum chamber), and $\theta = T - T_0$. In most cases, $\theta \ll T_0$, then we have: $Q_{\mathrm{rad}} \approx 8\varepsilon_{\mathrm{r}}\sigma WLT_0^3\theta$. Here the sample width W is much larger than its thickness D.

To eliminate heat convection, the sample is measured in a vacuum chamber whose pressure is down to 2–3 mTorr (detected by a convection vacuum gauge, CVM211 Stinger, InstruTech). Ignoring the gas conduction and non-consistent heating and convection, which are negligible in our experiment, and converting the surface radiation to body cooling source, the heat transfer governing equation for the sample becomes:

$$\frac{1}{\alpha}\frac{\partial\theta(x,t)}{\partial t} = \frac{\partial^2\theta(x,t)}{\partial x^2} + \frac{I^2R_0}{kLA_{\mathrm{c}}} + \frac{1}{k}\frac{8\varepsilon_{\mathrm{r}}\sigma T_0^3}{D}\theta, \quad (2)$$

with α the thermal diffusivity , k the thermal conductivity and A_{c} the cross-sectional area. I is the current passing through the sample and R_0 is the resistance of the sample before heating. The solution to the partial differential equation (2) can be obtained by an integral of Green's function [47]. More details regarding the solution are provided in [48]. After careful numerical and mathematic studies, with the effective thermal diffusivity $\alpha_{\mathrm{eff}} = \alpha(1 - f)$, where f is defined as $-8\varepsilon_{\mathrm{r}}\sigma T_0^3L^2/D\pi^2k$, the normalized average temperature rise T^* can be expressed as:

$$T^* \cong \frac{48}{\pi^4}\sum_{m=1}^{\infty}\frac{1-(-1)^m}{m^2}\frac{1-\exp[-m^2\pi^2\alpha_{\mathrm{eff}}t/L^2]}{m^2}. \quad (3)$$

The voltage evolution (V_{sample}) recorded by the oscilloscope is directly related to the average temperature change of the sample as:

$$\begin{aligned} V_{\mathrm{sample}} &= IR_0 + I\eta\frac{4q_0L^2}{k\pi^4} \\ &\quad\times\sum_{m=1}^{\infty}\frac{1-(-1)^m}{m^2}\frac{1-\exp[-m^2\pi^2\alpha_{\mathrm{eff}}t/L^2]}{m^2}. \end{aligned} \quad (4)$$

q_0 is the electrical heating power per unit volume and is constant during the measurement. η is the temperature coefficient of resistance of the sample. It is clear that the measured voltage change is inherently related to the temperature change of the sample. In our work, after T^*_{exp} is obtained, different trial values of α_{eff} are used to calculate the theoretical T^* using equation (3) and fit the experimental results (T^*_{exp}). The value giving the best fit of T^*_{exp} is taken as the thermal diffusivity of the sample. From equation $\alpha_{\mathrm{eff}} = \alpha(1 - f)$, we can get:

$$\alpha_{\mathrm{eff}} = \alpha + \frac{1}{\rho c_{\mathrm{p}}}\frac{8\varepsilon_{\mathrm{r}}\sigma T_0^3}{D}\frac{L^2}{\pi^2}. \quad (5)$$

This equation demonstrates that the measured thermal diffusivity has a linear relation to the effect of radiation. Such a theoretical background will be used later to subtract the radiation effect.

4. Thermal transport in graphene foams

4.1. Measurement of thermal diffusivity using the TET technique

First we take sample 1 as an example to detail how the thermal diffusivity is characterized. The sample is 1.74 mm wide and 0.87 mm thick. When it is cut into a 3.91 mm length, its electrical resistances before and after applying the step current are 17.2 and 16.9 Ω; the current used in the experiment is 62 mA, giving a voltage decrease change of about 1.7%. Figure 2(c) shows the transient voltage change of the raw experimental data. The normalized temperature rise $T^*(t)$ is determined from $T^*_{\mathrm{exp}} = (V_{\mathrm{sample}} - V_0)/(V_1 - V_0)$, where V_0 and V_1 are the initial and final voltages across the sample, and the fitting result is shown in figure 2(d). Its effective thermal diffusivity is determined as 6.07×10^{-5} m^2 s^{-1}, which includes the effect of radiation. We vary the trial values of α to determine the fitting uncertainty, as shown in figure 2(d). When the trial value is changed by 6%, the fit can be seen to deviate from the experimental results substantially.

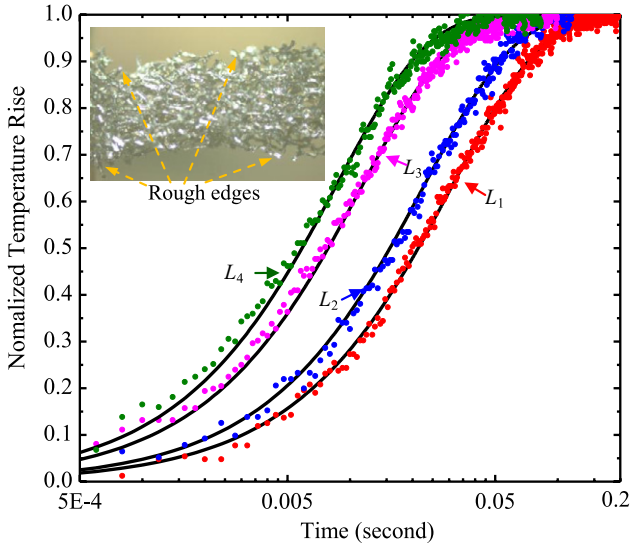

Figure 3. Comparisons between theoretical fitting and experimental data for the normalized temperature rise versus time for sample 4 at different lengths: $L_1 = 6.06$ mm, $L_2 = 5.00$ mm, $L_3 = 3.22$ mm, $L_4 = 2.54$ mm. The fitted thermal diffusivities are plotted in figure 4(d). These experiments are conducted under a pressure of about 2.8 mTorr. Dots are the experimental data and solid lines are the fit to the data. The inset shows an optical microscopy image of sample 4 connected between two electrodes.

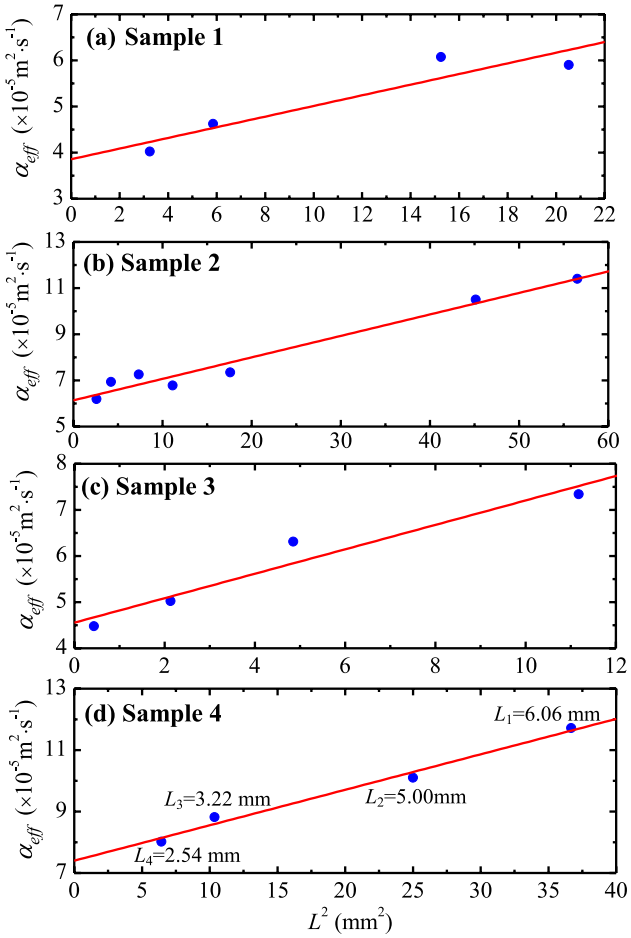

Figure 4. Linear fitting of the effective thermal diffusivity change against L^2 for GF samples 1–4. Dots are the experimental results and solid lines are the linear fitting.

So the uncertainty is determined as ±6%. The calibration result of one GF sample (1.10 mm wide, 4.17 mm long and 0.87 mm thick) is displayed in figure 2(d) (inset), in which the resistance increases from 16.2 to 16.7 Ω while the temperature decreases from 313 to 300 K. A linear fit is established based on the recorded data. If the temperature T does not vary too much, a linear approximation is typically used to describe the relationship between resistance and temperature: $R = R_0[1+\eta(T-T_0)]$, where T_0 (293 K) is room temperature, R_0 is the resistance at temperature T_0 and η is the temperature coefficient of resistance for the GF sample, determined as $-0.00\,234$ K^{-1}. For sample 1 of 3.91 mm length, during the experiment, a 62 mA DC is fed through it. The resistance change was −0.3 Ω and the consequent temperature rise is estimated as 7.41 K.

In order to eliminate the effect of radiation, the same GF sample is measured with its length (L) varying from long to short. As indicated in equation (5), the radiation effect is proportional to L^2. As the thermal diffusivity without the radiation effect (α) of the same sample from long to short is constant, the measured thermal diffusivity has a linear relation to L^2. Taking sample 4 as an example, after four repeated TET experiments we obtain four different measured thermal diffusivities varying with L^2. Figure 3 shows a comparison between the theoretical fits and experimental data for the normalized temperature rise for sample 4 of different lengths. By fitting the measured thermal diffusivity variation against L^2, the thermal diffusivity without the effect of radiation can be determined by extrapolation to the point $L = 0$. Figure 4(d) shows the linear fit of the effective thermal diffusivity change against L^2 for sample 4. By linear fitting of the data points and extending the fitting line to the y axis, we obtain an intersection point value of 7.40×10^{-5} m^2 s^{-1}, which is the thermal diffusivity without the radiation effect for the GF, because at this point ($L^2 \to 0$) there is no radiation. Using the same method, the thermal diffusivity without the radiation effect for other GF samples can be characterized, as shown in figures 4(a)–(c). For the other three samples, their thermal diffusivities without the radiation effect are 3.86×10^{-5}, 6.14×10^{-5} and 4.56×10^{-5} m^2 s^{-1} for sample 1–3, respectively.

It can be seen from equation (5) that the effective thermal diffusivity (α_{eff}) changes linearly with the square of length (L^2) and the slope (ψ) of the fitting line is $8\varepsilon_r\sigma T_0^3/(\rho c_p)_e D\pi^2$, where D is the thickness of the graphene foam and $(\rho c_p)_e$ is the effective heat capacity of the sample. The numerator of this term is proportional to the surface radiation, and the denominator is proportional to the heat capacity of the graphene foam. This term can also be expressed as $8\varepsilon\sigma T_0^3/\rho c_p \delta\pi^2$, where ρ and c_p are the intrinsic density and specific heat of the graphene, ε the emissivity of the graphene surface under the effect of flake-to-flake scattering, and δ the thickness of the two-layer graphene (0.67 nm). The slopes of the fitting lines are determined as 1.16, 0.93, 2.65 and 1.15 s^{-1} for samples 1–4 (shown in figure 4). As the other parameters are all known, the effective emissivity

of graphene can be calculated as 0.11%, 0.09%, 0.25% and 0.11% for samples 1–4. Freitag *et al* [49] found a wavelength-independent emissivity of $\varepsilon = (1.6 \pm 0.8)\%$ in the near-infrared region for SLG, in reasonable agreement with measurements of optical absorption [50]. However, references about the emissivity in the far-infrared region for SLG are scarce. Dawlaty *et al* [51] measured the optical absorption spectra of epitaxial graphene from the terahertz to the visible frequencies. Based on their result, SLG over the infrared spectrum of 10 μm should have an emissivity around 0.238% from one side. The graphene in our samples is two-layer. To a first-order estimate, the emissivity is around 0.476% from one side without considering the radiation reflection between layers. The actual value of emissivity should be smaller than 0.476%. Our measured emissivity is less than this value. Such a difference is largely attributed to the interference among graphene flakes (scattering, absorption and reflection). Edges, defects and impurities in the sample will all give variations in the emissivity from sample to sample.

4.2. Intrinsic thermal diffusivity and conductivity of graphene

In order to determine the intrinsic thermal diffusivity and conductivity of graphene, the model of Schuetz *et al* [52] for the thermal conductivity of porous media is used. The intrinsic thermal conductivity of graphene k_G is:

$$k_G = 3k_{GF}/\varphi. \tag{6}$$

φ is the volume fraction of the solid phase in the foam, which is very small in our GF sample. k_{GF} is the effective thermal conductivity of GF. Krishnan *et al* [53] have confirmed the correlation between the effective thermal conductivity and effective thermal conductivity expressed by equation (6) is accurate in open-celled metal foams at low φ (lower than 6%). This condition applies well to our GF samples. Pettes *et al* [36] also used this model to determine the thermal conductivity of the FLG and UG constituents inside the GF.

Dividing both sides of equation (6) by the heat capacity of graphene $[(\rho c_p)_G]$ transforms equation (6) to $\alpha_G = 3\alpha_{GF}$, where α_G and α_{GF} are the thermal diffusivity of graphene and the GF as $\alpha_G = k_G/(\rho c_p)_G$ and $\alpha_{GF} = k_{GF}/(\rho c_p)_{GF}$. Here we have $(\rho c_p)_{GF} = (\rho c_p)_G \varphi$. As can be seen here, without knowing the volume fraction (porosity) of the GF sample, φ, the intrinsic thermal diffusivity of graphene can be directly determined from the effective thermal diffusivity of the GF sample. This provides a great advantage in studying the thermal transport capacity of graphene with good accuracy. For this reason, the intrinsic thermal diffusivity of graphene (α_G) is calculated as 1.16×10^{-4} m^2 s^{-1} for sample 1. Without losing accuracy, using the density and specific heat of graphite for the graphene calculation ($\rho = 2210$ kg m^{-3}, $c_p = 709$ J (kg K)$^{-1}$ [54]), the intrinsic thermal conductivity can be obtained from the equation $k = \alpha \rho c_p$ as 182 W m^{-1} K^{-1} for sample 1. Results are detailed in table 1 for the other samples. It is evident that the thermal diffusivity and conductivity vary from sample to sample. The intrinsic thermal diffusivity of all GF samples varies from 1.16×10^{-4} to 2.22×10^{-4} m^2 s^{-1}. Also the intrinsic thermal conductivity ranges from 182 to 349 W m^{-1} K^{-1}. It should be pointed out that our intrinsic thermal conductivity results are obtained without using the parameter φ, which means that errors in the thermal characterization due to uncertainty in φ are avoided. Pettes *et al* [36] measured the thermal conductivity of GF—then based on the theoretical model the solid thermal conductivity of the FLG and UG constituents were obtained. An uncertainty of about 10–20% exists in their results, which is mainly due to the uncertainty in φ.

Table 1. Details of the results for GF samples characterized using the TET technique.

Sample	α_{real} ($\times 10^{-5}$ m^2 s^{-1})	α_{intr} ($\times 10^{-4}$ m^2 s^{-1})	Thermal conductivity of graphene (W m^{-1} K^{-1})
1	3.86	1.16	182
2	6.14	1.84	289
3	4.56	1.37	215
4	7.40	2.22	349

From another point of view, that the correlation (factor 3) between α_G and α_{GF} is reliable in open-celled metal foams at low φ is demonstrated as follows. In data processing for the TET experiment, the apparent length of the GF sample is used. However, it is not the actual route of heat transfer since the graphene is not straight in GF. Figure 5 shows parts of the heat transfer path evaluation for GF samples 1 and 2 in two dimensions. Taking sample 1 in figure 5(a) as an example, between points A and B the heat transfer should follow paths 1 or 2, as we indicate in the figure, and these paths are much longer than the straight line connecting points A and B. It should be pointed out that there are many paths from point A to B, and we only show two of them here. In addition to the heat transfer paths evaluation shown in figure 5, we conducted many other heat transfer path evaluations. After considering all the heat transfer path evaluations, the average ratios of the actual heat transfer route over the straight length are 1.50 and 1.19 for samples 1 and 2, respectively. In fact, the intrinsic ratio of the actual heat transfer route over the straight length is larger than that observed in the 2D picture, as GF has a three-dimensional network. Taking the isotropous property of GF into consideration, owing to $\sqrt{L_x^2 + L_y^2} = 1.55$ and 1.19, we can obtain the ratios of the actual heat transfer route versus the straight length as $\sqrt{L_x^2 + L_y^2 + L_z^2} = 1.90$ and 1.46 for samples 1 and 2, respectively. Using the same method, the ratio of the actual heat transfer route over the straight length is estimated as 1.43 for samples 3 and 4, respectively. Since the thermal diffusivity $\alpha \sim 0.2026L^2/t$, the ratios of α_G to α_{GF} are calculated as 2.05–3.61 for samples 1–4. This factor range: 2.05–3.61 agrees well with the factor 3 used in Schuetz's model.

4.3. Physics behind the strong thermal conductivity reduction

The thermal diffusivity and thermal conductivity of GF from our measurement varies significantly from sample to sample, as inside the foam there are many spherical pores with small

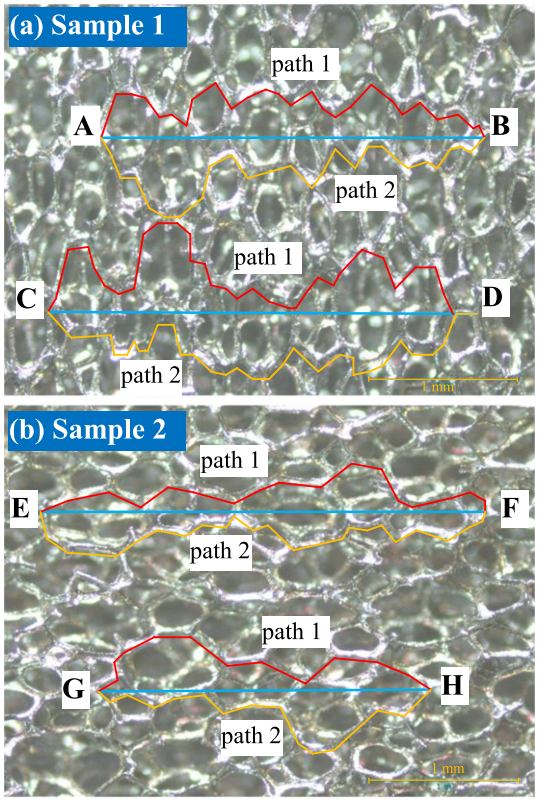

Figure 5. Part of the heat transfer path evaluation for (a) sample 1 and (b) sample 2. The blue line is the straight length. The red and yellow lines are path 1 and path 2 of actual heat transfer path. The average ratios of the actual heat transfer route over the straight length are 1.45, 1.56, 1.18 and 1.21 for paths AB, CD, EF and GH, respectively.

openings (their size around 200–500 μm) and all samples were cut from one large piece of sample. It is inevitable that rough edges will be left and the shapes of the edges will differ from each other. The intrinsic thermal conductivity of graphene varies from 182 to 349 W m^{-1} K^{-1}, much lower than values reported for SLG: 1500–5800 W m^{-1} K^{-1} [24, 26, 55] and FLG ($n = 2$–4): 1300–2800 W m^{-1} K^{-1} [15]. Wei *et al* [56] investigated the in-plane thermal conductivity of multilayer graphene films using nonequilibrium molecular dynamics simulations. They found the thermal conductivity of five-layer graphene is about 580 W m^{-1} K^{-1} at RT, which is close to the value of graphite. The mechanisms behind this reduction are outlined as follows. First, a certain amount of corrugation and folding is clearly observed on the surface of the graphene, as shown in figure 1(c). The observed thermal conductivity reduction is partly attributed to this wrinkled surface structure. Phonons cannot pass through the wrinkled surface and will scatter on it. From figure 1(f), it is measured that the typical size of the graphene flakes is from 2.38 to 5.14 μm. On joints and interfaces of graphene flakes, strong phonon scattering will occur. Second, rough edges are another reason for the small thermal conductivity. The sample we purchased is 1 cm × 1 cm square. When it is prepared for TET measurement, it is cut into a small piece using a blade. It is inevitable that rough edges will be left. The inset of figure 3 shows the rough edges of sample 4. Very strong phonon scattering can occur at the rough edges. Last but not least, it is clear in figure 1(e) that the high magnification SEM picture shows that some dots are distributed on top of the graphene surface. The average distance between dots is about 127 nm, which is much smaller than the average phonon mean free path (775 nm) in bulk crystalline graphene [23], indicating strong structural defects. This will give strong phonon scattering from these impurity dots, leading to a lower thermal conductivity. Pettes *et al* [36] found the solid thermal conductivity values of GF are from 176 ± 37 to 995 ± 162 W m^{-1} K^{-1} at RT. They explained that the phonon transport in the GF is limited only by the unfolded crystallite domain size at low temperature and phonon–phonon scattering in the FLG/UG building blocks near room temperature.

5. Conclusion

In summary, the thermal diffusivity of suspended GF was characterized using the TET method. The effective thermal diffusivity of the GF samples was measured as 3.86–7.40 × 10^{-5} m^2 s^{-1}. After considering the non-straight feature of graphene network structure in the foam, the intrinsic thermal diffusivity is calculated as 1.16–2.22 × 10^{-4} m^2 s^{-1}. This intrinsic thermal diffusivity determination does not need porosity knowledge of the GF, resulting in a highly accurate result. The results showed that the intrinsic thermal conductivity of the suspended graphene is about 182–349 W m^{-1} K^{-1} at RT, around one order of magnitude lower than those reported for single-layer graphene. This substantial reduction is attributed to very strong phonon scattering at grain boundaries, defects and rough edges of the GF.

Acknowledgments

Support of this work from the Office of Naval Research (N000141210603), Army Research Office (W911NF-12-1-0272), and National Science Foundation (CBET-0931290, CBET-1235852) is gratefully acknowledged. H L is supported by the China Scholarship Council for a two-year study at Iowa State University. N M is grateful for support from the National Natural Science Foundation of China (NSFC: 51076146). X W is grateful for support from the 'Eastern Scholar' Program of Shanghai.

References

[1] Geim A K 2009 Graphene: status and prospects *Science* **324** 1530–4
[2] Geim A K and Novoselov K S 2007 The rise of graphene *Nature Mater.* **6** 183–91
[3] Zhang Y B, Tan Y W, Stormer H L and Kim P 2005 Experimental observation of the quantum Hall effect and Berry's phase in graphene *Nature* **438** 201–4
[4] Balandin A A, Ghosh S, Bao W Z, Calizo I, Teweldebrhan D, Miao F and Lau C N 2008 Superior thermal conductivity of single-layer graphene *Nano Lett.* **8** 902–7

[5] Stoller M D, Park S J, Zhu Y W, An J H and Ruoff R S 2008 Graphene-based ultracapacitors *Nano Lett.* **8** 3498–502

[6] Lee C, Wei X D, Kysar J W and Hone J 2008 Measurement of the elastic properties and intrinsic strength of monolayer graphene *Science* **321** 385–8

[7] Schwierz F 2010 Graphene transistors *Nature Nanotechnol.* **5** 487–96

[8] Kim K S, Zhao Y, Jang H, Lee S Y, Kim J M, Kim K S, Ahn J H, Kim P, Choi J Y and Hong B H 2009 Large-scale pattern growth of graphene films for stretchable transparent electrodes *Nature* **457** 706–10

[9] Huang Y X, Dong X C, Liu Y X, Li L J and Chen P 2011 Graphene-based biosensors for detection of bacteria and their metabolic activities *J. Mater. Chem.* **21** 12358–62

[10] Zhu Y W *et al* 2011 Carbon-based supercapacitors produced by activation of graphene *Science* **332** 1537–41

[11] Yu D S, Park K, Durstock M and Dai L M 2011 Fullerene-grafted graphene for efficient bulk heterojunction polymer photovoltaic devices *J. Phys. Chem. Lett.* **2** 1113–8

[12] Huang X, Qi X Y, Boey F and Zhang H 2012 Graphene-based composites *Chem. Soc. Rev.* **41** 666–86

[13] Novoselov K S, Jiang Z, Zhang Y, Morozov S V, Stormer H L, Zeitler U, Maan J C, Boebinger G S, Kim P and Geim A K 2007 Room-temperature quantum Hall effect in graphene *Science* **315** 1379

[14] Balandin A A 2011 Thermal properties of graphene and nanostructured carbon materials *Nature Mater.* **10** 569–81

[15] Ghosh S, Bao W Z, Nika D L, Subrina S, Pokatilov E P, Lau C N and Balandin A A 2010 Dimensional crossover of thermal transport in few-layer graphene *Nature Mater.* **9** 555–8

[16] Ghosh S, Nika D L, Pokatilov E P and Balandin A A 2009 Heat conduction in graphene: experimental study and theoretical interpretation *New J. Phys.* **11** 095012

[17] Xu H L, Zhang Z Y, Wang Z X, Wang S, Hang X L and Peng L M 2011 Quantum capacitance limited vertical scaling of graphene field-effect transistor *ACS Nano* **5** 2340–7

[18] Yan Z, Liu G X, Khan J M and Balandin A A 2012 Graphene quilts for thermal management of high-power GaN transistors *Nature Commun.* **3** 827

[19] Veca L M, Meziani M J, Wang W, Wang X, Lu F S, Zhang P Y, Lin Y, Fee R, Connell J W and Sun Y P 2009 Carbon nanosheets for polymeric nanocomposites with high thermal conductivity *Adv. Mater.* **21** 2088–92

[20] Shahil K M F and Balandin A A 2012 Graphene-multilayer graphene nanocomposites as highly efficient thermal interface materials *Nano Lett.* **12** 861–7

[21] Yu W, Xie H Q and Chen W 2010 Experimental investigation on thermal conductivity of nanofluids containing graphene oxide nanosheets *J. Appl. Phys.* **107** 094317

[22] Gupta S S, Siva V M, Krishnan S, Sreeprasad T S, Singh P K, Pradeep T and Das S K 2011 Thermal conductivity enhancement of nanofluids containing graphene nanosheets *J. Appl. Phys.* **110** 084302

[23] Ghosh S, Calizo I, Teweldebrhan D, Pokatilov E P, Nika D L, Balandin A A, Bao W, Miao F and Lau C N 2008 Extremely high thermal conductivity of graphene: prospects for thermal management applications in nanoelectronic circuits *Appl. Phys. Lett.* **92** 151911

[24] Chen S S *et al* 2011 Raman measurements of thermal transport in suspended monolayer graphene of variable sizes in vacuum and gaseous environments *ACS Nano* **5** 321–8

[25] Wang Z Q, Xie R G, Bui C T, Liu D, Ni X X, Li B W and Thong J T L 2011 Thermal transport in suspended and supported few-layer graphene *Nano Lett.* **11** 113–8

[26] Lee J U, Yoon D, Kim H, Lee S W and Cheong H 2011 Thermal conductivity of suspended pristine graphene measured by Raman spectroscopy *Phys. Rev.* B **83** 081419(R)

[27] Seol J H *et al* 2010 Two-dimensional phonon transport in supported graphene *Science* **328** 213–6

[28] Lindsay L, Broido D A and Mingo N 2011 Flexural phonons and thermal transport in multilayer graphene and graphite *Phys. Rev.* B **83** 235428

[29] Hu J N, Ruan X L and Chen Y P 2009 Thermal conductivity and thermal rectification in graphene nanoribbons: a molecular dynamics study *Nano Lett.* **9** 2730–5

[30] Lan J H, Wang J S, Gan C K and Chin S K 2009 Edge effects on quantum thermal transport in graphene nanoribbons: tight-binding calculations *Phys. Rev.* B **79** 115401

[31] Chen Z P, Ren W C, Gao L B, Liu B L, Pei S F and Cheng H M 2011 Three-dimensional flexible and conductive interconnected graphene networks grown by chemical vapour deposition *Nature Mater.* **10** 424–8

[32] Fan D Q, Liu Y, He J P, Zhou Y W and Yang Y L 2012 Porous graphene-based materials by thermolytic cracking *J. Mater. Chem.* **22** 1396–402

[33] Zhao Y Q, Zhao D D, Tang P Y, Wang Y M, Xu C L and Li H L 2012 MnO_2/graphene/nickel foam composite as high performance supercapacitor electrode via a facile electrochemical deposition strategy *Mater. Lett.* **76** 127–30

[34] Yavari F, Chen Z P, Thomas A V, Ren W C, Cheng H M and Koratkar N 2011 High sensitivity gas detection using a macroscopic three-dimensional graphene foam network *Sci. Rep.-UK* **1** 166

[35] Zhou X F and Liu Z P 2011 Graphene foam as an anode for high-rate Li-ion batteries *IOP Conf. Ser.: Mater. Sci. Eng.* **18** 062006

[36] Pettes M T, Ji H X, Ruoff R S and Shi L 2012 Thermal transport in three-dimensional foam architectures of few-layer graphene and ultrathin graphite *Nano Lett.* **12** 2959–64

[37] Hodkiewicz J 2010 *Characterizing Graphene with Raman Spectroscopy* Thermo Scientific application note

[38] Graf D, Molitor F, Ensslin K, Stampfer C, Jungen A, Hierold C and Wirtz L 2007 Spatially resolved Raman spectroscopy of single-and few-layer graphene *Nano Lett.* **7** 238–42

[39] Howe J Y, Rawn C J, Jones L E and Ow H 2003 Improved crystallographic data for graphite *Powder Diffr.* **18** 150–4

[40] Cao A Y, Xu C L, Liang J, Wu D H and Wei B Q 2001 X-ray diffraction characterization on the alignment degree of carbon nanotubes *Chem. Phys. Lett.* **344** 13–7

[41] Guo J Q, Wang X W and Wang T 2007 Thermal characterization of microscale conductive and nonconductive wires using transient electrothermal technique *J. Appl. Phys.* **101** 063537

[42] Guo J Q, Wang X W, Zhang L J and Wang T 2007 Transient thermal characterization of micro/submicroscale polyacrylonitrile wires *Appl. Phys.* A **89** 153–6

[43] Feng X, Wang X, Chen X and Yue Y 2011 Thermo-physical properties of thin films composed of anatase TiO_2 nanofibers *Acta Mater.* **59** 1934–44

[44] Feng X H, Huang X P and Wang X W 2012 Thermal conductivity and secondary porosity of single anatase TiO_2 nanowire *Nanotechnology* **23** 185701

[45] Feng X H and Wang X W 2011 Thermophysical properties of free-standing micrometer-thick poly (3-hexylthiophene) films *Thin Solid Films* **519** 5700–5

[46] Huang X P, Wang J M, Eres G and Wang X W 2011 Thermophysical properties of multi-wall carbon nanotube bundles at elevated temperatures up to 830 K *Carbon* **49** 1680–91

[47] Beck J V, Cole K D, Haji-Sheikh A and Litkouhi B (ed) 1992 *Heat Conduction Using Green's Functions* (New York: Hemisphere) p 482

[48] Liu G Q, Lin H, Tang X D, Bergler K and Wang X W 2013 Characterization of thermal transport in one-dimensional solid materials *J. Vis. Exp.* at press

[49] Freitag M, Chiu H Y, Steiner M, Perebeinos V and Avouris P 2010 Thermal infrared emission from biased graphene *Nature Nanotechnol.* **5** 497–501

[50] Nair R R, Blake P, Grigorenko A N, Novoselov K S, Booth T J, Stauber T, Peres N M R and Geim A K 2008 Fine structure constant defines visual transparency of graphene *Science* **320** 1308

[51] Dawlaty J M, Shivaraman S, Strait J, George P, Chandrashekhar M, Rana F, Spencer M G, Veksler D and Chen Y Q 2008 Measurement of the optical absorption spectra of epitaxial graphene from terahertz to visible *Appl. Phys. Lett.* **93** 131905

[52] Schuetz M A and Glicksman L R 1984 A basic study of heat-transfer through foam insulation *J. Cell. Plast.* **20** 114–21

[53] Krishnan S, Murthy J Y and Garimella S V 2006 Direct simulation of transport in open-cell metal foam *Trans. ASME, J. Heat Transfer* **128** 793–9

[54] Incropera F P 2007 *Fundamentals of Heat and Mass Transfer* (Hoboken, NJ: Wiley) p 933

[55] Cai W W, Moore A L, Zhu Y W, Li X S, Chen S S, Shi L and Ruoff R S 2010 Thermal transport in suspended and supported monolayer graphene grown by chemical vapor deposition *Nano Lett.* **10** 1645–51

[56] Wei Z Y, Ni Z H, Bi K D, Chen M H and Chen Y F 2011 In-plane lattice thermal conductivities of multilayer graphene films *Carbon* **49** 2653–8